

Gas Physisorption Measurements as a Quality Control Tool for the Properties of Graphene/Graphite Powders

Sofia Marchesini¹, Piers Turner¹, Keith R. Paton¹, Benjamin P. Reed¹, Barry Brennan¹, Krzysztof Koziol² and Andrew J. Pollard¹
*

¹ National Physical Laboratory, Hampton Road, Teddington, TW11 0LW, UK

² Enhanced Composites and Structures Centre, School of Aerospace, Transport and Manufacturing, Cranfield University, Bedfordshire MK43 0AL, UK

Corresponding Author. Tel: +442089436266; E-mail: andrew.pollard@npl.co.uk

Keywords: graphene, 2D materials, layers, nitrogen physisorption, specific surface area

The industrial-scale production and commercialisation of graphene and related 2D materials introduces the need for rapid, reliable and cost-effective quality control procedures. Currently, microscopy-based techniques are used to measure the lateral size and thickness of particles but while powerful, these techniques suffer from limitations such as lengthy analysis time, high costs and limited sampling. In the case of carbon-based 2D materials, as the stacking of multiple graphene sheets causes a reduction in the surface to mass ratio, the number of layers can hypothetically be calculated by comparing the theoretical surface area of monolayer graphene ($2630 \text{ m}^2/\text{g}$) to the calculated specific surface area (SSA) measured by gas physisorption measurements. However, despite the potential of this method of analysis, there is limited understanding regarding the characterisation of commercial graphene/graphite powders produced

via bottom-up and top-down methods. Herein, the SSAs of a variety of commercially-available graphitic powders were measured using nitrogen physisorption isotherms at 77 K and applying Brunauer-Emmett-Teller theory. The as-obtained SSAs were then correlated to the structural and chemical properties of the materials (obtained using conventional techniques) to demonstrate the suitability of this measurement technique for quality control of graphitic powders.

1. Introduction Graphene, a two-dimensional (2D) material composed of a single layer of carbon atoms with an sp^2 hybridisation,[1] was initially predicted to be thermodynamically unstable [2,3] until its existence was demonstrated by Geim and Novoselov using the “scotch-tape” method.[4] Since its discovery, interest in graphene has grown exponentially due to its unique theoretical properties [5] and potential applications.[6,7] As a result, research efforts into the development of industrial-scale techniques for the production of graphene are ongoing [8–12] and the number of companies seeking to produce commercial graphene materials is increasing, with a reported total annual production of 400 tonnes in China alone.[10,13] However, properties of commercial “graphene” often differ greatly from high-quality graphene sheets produced *via* chemical vapour deposition or mechanical cleavage of graphite.[3, 5,14,15] In fact, Kauling *et al.* [16] recently concluded that many products sold as “graphene” are actually highly priced graphite powders. The features of these commercially produced graphitic materials, such as the number of layers, lateral flake size and level of disorder, are known to vary significantly. Therefore, there is a clear need for the development of international measurement standards and quality control procedures.[1,17,18] (see also ISO TS 80004-13:2017)

Currently, no standalone technique can be used to characterise the number of layers in bulk materials (e.g. powders) in a fast and reliable manner. Electron microscopy techniques, such as scanning electron microscopy (SEM), are often used in combination with scanning probe

microscopy techniques, e.g. atomic force microscopy (AFM), to characterise the lateral flake size and flake thickness of graphitic materials.[19] However, these techniques only characterise individual particles which makes them extremely time consuming and expensive, therefore, they cannot be implemented as fast quality control procedures available to the industry on the factory floor. Raman spectroscopy is often employed for the characterisation of not only the level of disorder in carbon-based materials, but also the number of layers, lateral flake size, and number of edge and basal plane defects. [19–21] However, data interpretation for poly-dispersed graphitic materials is often only qualitative and complicated to perform.

An indirect approach to estimate the number of graphitic layers is *via* the measurement of the specific surface area (SSA). A single atom-thick graphene sheet has a theoretical surface area of 2630 m²/g, nearly independent of the lateral size of the graphene flakes.[22] As layers are stacked to form non-porous graphitic materials, the specific surface area (S) is expected to decrease proportionately with increasing number of layers (N) such that $S = (2630/N)$ m²/g. Ohba *et al.* demonstrated *via* simulation that this equation applies to graphitic materials down to 2 layers, however, the authors suggested that in real graphitic materials it may not always be applicable due to the presence of amorphous carbon and additional impurities. [22] The SSA is typically measured by applying Braunauer-Emmett-Teller (BET) theory [23] to gas physisorption isotherms. Gas physisorption offers several advantages over microscopy techniques, such as: faster analysis times, a larger sample population and good repeatability. Additionally, the measurement of SSA using the BET method satisfies the requirement for 2020 REACH registration of “nanoforms” substances and thus for the use of “graphene” materials throughout the entire European Economic Area. [24]

However, analysis requires dry samples, which may cause aggregation, especially for graphene dispersions produced *via* LPE. Contrasting reports can be found in the literature regarding the reliability of BET analysis for estimating the average number of graphitic layers. For example, Guo *et al.* hypothesised that graphitic materials can maintain their BET SSA due to irregular agglomeration of platelets, leading to regular mesopores with dimensions that were equivalent to multiples of the average platelet thickness.[25] Li *et al.*, on the other hand, showed that the SSA of graphitic materials could not be directly correlated to the number of 2D layers present, due to re-aggregation of the samples produced by LPE methods.[26] Additional research showed that re-aggregation could be reduced by adding an intercalating agent, keeping graphene sheets apart. Intercalating agents include polyvinylpyrrolidone powder (SSA=760 m²/g)[27], iron chloride (SSA=217 m²/g) [28], platinum nanoparticles (SSA=862 m²/g) compared to an SSA of 44 m²/g without additive [29] or pillaring with carbon black for graphene oxide (GO) materials (SSA=1006 m²/g) compared to an SSA of 38 m²/g without additive. [25] Attempts have also been made to measure the surface area of graphitic materials in dispersions through the adsorption of methylene blue, which could prevent potential aggregation upon drying. [30–32] Surface areas calculated from methylene blue adsorption were generally reported to be higher than the standard BET SSA, suggesting re-aggregation of the materials in dry form. However, the use of methylene blue for estimating the surface area is unreliable, as the adsorption capacity does not solely depend upon the surface area, but also the chemistry of the material. [33,34]

The presence of defects and by-products (such as amorphous carbon) in graphitic materials represents another issue in the application of BET SSA for the determination of the average number of layers. These features may introduce micropores within the material and, therefore,

increase the surface area independent of the average number of layers. For example, activated carbons and reduced GO (rGO) can exhibit surface areas in excess of 3000 m²/g.[35–37]

Thermally or chemically reduced GO materials, are well known to contain many nanoscale defects (vacancy defects and *sp*³-hybridised carbon), deriving from the large amount of oxygen impurities introduced during oxidation, disrupting the carbon lattice. The BET SSA of rGO is generally reported to be high (usually in large excess of 200 m²/g) [31,38–43] and can be further increased by varying the parameters employed during reduction.[44–46] Interestingly, however, GO usually exhibits a relatively low SSA (roughly around 30-50 m²/g) compared to rGO, with the results of the former attributed to ordered re-stacking when dry, despite containing a large amount of defects. [25, 44,47] Guo *et al.* hypothesised that GO materials exhibit lower plate rigidity compared to few-layer graphene, leading to ordered re-stacking. [25]

Graphene produced *via* ball-milling also commonly exhibits many defects due to the impact forces of steel grinding balls onto the graphite sheets.[47] Chen *et al.* [48] showed that graphene produced by dry ball-milling has higher surface area (> 500 m²/g) compared to wet ball-milling (100 m²/g), in which impact forces are reduced due to the presence of a fluid.

A recent paper published by Kovtun *et al.* [49] benchmarked commercial graphitic materials characterised with nitrogen physisorption and traditional techniques (static light scattering, Raman and X-ray photoelectron spectroscopy (XPS), and Scott volumeter for bulk density measurement). It was shown that samples with lower *sp*³ carbon content (measured by peak fitting the C 1s XPS spectra), generally exhibited low BET SSA. However, the number of layers of graphitic materials was solely deduced from the BET SSA measured and was not confirmed using other techniques. Guo *et al.* also employed BET analysis to estimate the average number of layers in graphitic

materials and compared them to those reported by the manufacturer, however, no independent technique was employed to verify the number of layers. [25]

Clearly, despite physisorption analysis providing some useful information regarding the BET SSA and pore structure of samples, more research is needed in order to determine its reliability in estimating the average number of layers and level of disorder of graphitic powders.

In this study, several commercially-available powders advertised as ‘graphene’ in their description, were characterised as received through nitrogen physisorption (BET SSA measured) and compared to the results obtained from microscopy (AFM and SEM), and spectroscopic (Raman spectroscopy, XPS) techniques. Samples were chosen to include commercially available materials produced through common production techniques such as LPE, ball-milling and bottom-up methods. A correlation is shown between the ratio of non-graphitic/graphitic carbon in the materials and the BET SSA, as well as the size of the particles, highlighting the potential of this technique as a quality control tool for the characterisation of graphitic powders. The importance of understanding the type of graphitic material under investigation and therefore the accuracy in the BET SSA measurement is also discussed and demonstrated.

2. Materials and Methods

2.1. Materials

Commercial graphitic powder materials were sourced from a range of suppliers (**Table 1**).

Definitions employed here (according to ISO/TS 80004-2:2015(en)):

- Particle: “minute piece of matter with defined physical boundaries”;
- Primary particle: “original source particle of agglomerates or aggregates or mixtures of the two”;

- Agglomerate: “collection of weakly or medium strongly bound particles where the resulting external surface area is similar to the sum of the surface areas of the individual components”;
- Aggregate: “particle comprising strongly bonded or fused particles where the resulting external surface area is significantly smaller than the sum of surface areas of the individual components”.

Table 1 List of graphitic powders, producers and production methods

	Product, Producer	Production methods
G1*	Elicarb, Thomas Swan	Liquid-phase exfoliation
G2*	Elicarb, Thomas Swan	Liquid-phase exfoliation
G3	Haydale Ltd	Advanced milling technology
G4	Haydale Ltd	Mechanical exfoliation (ball-milling)
G5	G1, Cambridge Nanosystems	Microwave plasma bottom-up method
G6	G3, Cambridge Nanosystems	

*These materials were produced using one of the two exfoliation methods employed by Thomas Swan and one of the several grades commercially-available

Pellets of graphitic powders were produced for XPS and Raman spectroscopy measurements by mechanically pressing the powders in a small hydraulic handheld press (Specac, Orpington, UK) by applying a force of 1-2 tons onto a 7 mm diameter, round, pellet die. These pellets were then mounted on an aluminium sample holder using conductive carbon and copper tape, which could then be mounted directly on the XPS or Raman spectrometer sample stages.

Graphitic dispersions were prepared gravimetrically with a concentration of roughly 0.1 mg/g in dimethyl sulfoxide (DMSO, Reagent Grade 99.5 %, Fisher Scientific, UK) and were sonicated for 5 minutes in an ultrasonic bath at a frequency of 37 kHz and 80 W ultrasonic power (CamSonix C275T, Camlab, Cambridge, UK) to try to separate any aggregates/agglomerates and obtain the primary particles. The sonication time is kept short to minimise any structural changes to the as-received materials.[50] The dispersions (10 μ L) were then drop-cast on silicon wafers with a native

oxide layer at the boiling point of the solvent (roughly 189 °C) for SEM analyses. AFM samples were prepared on a silica/silicon substrate with a 300 nm thick oxide layer.

2.2. Methods

2.2.1. Structural characterisation

SEM – Powder samples were dispersed in a solvent and deposited onto a silica/silicon substrate as described in the materials section. Images were then collected using a Zeiss (Oberkochen, Germany) Supra Microscope by measuring secondary electrons (In lens detector, 30 µm aperture, 5 kV accelerating voltage). Images were then analysed using SPIP (Version 6.7.5, Image Metrology A/S, Denmark). The length and width of a minimum of 200 particles were measured and the lateral sizes were calculated as the mean of length and width. Origin (Origin(Pro), Version 2019b, OriginLab Corporation, Northampton, MA, USA) was then used to fit a lognormal distribution of lateral size for each sample, and the lognormal median was calculated for each sample and standard deviations for the mean were calculated from the spread of the data.

AFM – AFM measurements were performed using an Asylum Research MFP-3D in a 21°C temperature-controlled laboratory. The graphene samples were dispersed at a concentration of 0.1 mg/ml in DMSO and sonicated for 5 minutes in a sonic bath prior to deposition. 5 µl of the dispersion was drop-cast on to 10 mm × 10 mm silicon/silica wafers with a 300 nm wet thermal oxide that were pre-heated to 150 °C. The thickness of the graphitic particles was determined by analysing the apparent height of each feature from three horizontal profiles (along the scanning axis), and the uncertainty was recorded as the standard deviation in three values of thickness (unless this was less than the RMS roughness of the substrate, in which case the uncertainty is the RMS roughness). The uncertainty in the length and width of each particle was calculated from the size of the slope measured at the edges of each particle; due to the convolution of the sample and

the AFM probe-apex, there is not a sharply defined step between the substrate and the particle height. To obtain representative AFM thickness measurements, at least 20 isolated features were characterised across the lateral size distribution previously measured using SEM. Heights and lateral sizes derived from AFM were then plotted and fitted with a linear fit using Origin. The fitting parameters were selected without a fixed intercept, with a weighted fitting called ‘instrumental’ which employs a weighting formula of $(=1 / e_i^2)$, where e_i are the error bar sizes. The 95 % confidence interval for the fitting was also calculated employing OriginLab. AFM heights were then calculated by converting the SEM lognormal distributions into height distributions by employing the linear correlation found between lateral size and AFM height.

Nitrogen physisorption – Graphitic powder samples were employed as provided. A minimum of 100 mg of powder sample was loaded inside a long glass analysis tube (tubes were weighed empty and then filled with sample and weighed again) for each sample. Samples were degassed overnight (minimum of 12 hours) in an external degas unit FlowPrep (Micromeritics, UK) by flowing nitrogen gas (nitrogen (oxygen free), BOC, Surrey, UK) over the samples either at 130 °C or at 300 °C. A low nitrogen flow rate was employed to avoid aerosolisation of the powder samples. After the degas step was completed, samples were allowed to cool under flowing nitrogen gas. Samples were then re-weighed immediately after degassing and placed onto the sorption analyser (ASAP 2460, Micromeritics, UK) for gas sorption analysis. The samples were degassed *in-situ* down to at least 0.7 Pa with a low evacuation rate (roughly 0.1-0.2 kPa/s) at ambient temperature. Helium (helium (A grade), BOC, Surrey, UK) was employed to measure the free-space volume at the start of the analysis. All samples were re-degassed in the analyser at ambient temperature for 30 minutes after helium analysis. The analysis was then performed by employing nitrogen probing gas at liquid nitrogen temperature. The saturation pressure of nitrogen was measured at each

isothermal point. A minimum of 6 points were collected in the relative pressure range of 0.01-0.30 p/p_0 . The BET equation was then employed to measure the surface area from nitrogen sorption isotherms.[23] A molecular cross-sectional area of 0.1620 nm² was employed for nitrogen in the BET calculation.

The range of relative pressures over which BET theory was applied was chosen to obtain a: i) positive C value, ii) positive intercept, iii) a correlation coefficient greater than 0.9999 and iv) increasing $V \left(1 - \frac{P}{P_0}\right)$ with increasing $\frac{P}{P_0}$. [51] Each measurement was repeated at least 3 times and an average BET SSA was reported. The uncertainty was calculated from the standard deviation (σ) between individual measurements and reported as 3 σ .

External SSA (or non-micropore SSA) were calculated by applying i) the Harkins and Jura [52] and ii) the Magee Carbon Black STSA [53] (ASTM-D6556-10) t-plot equations to nitrogen physisorption isotherms.

i) Harkins and Jura t-plot equation:
$$t \text{ (nm)} = 0.1 \left[\frac{13.99}{0.034 - \log_{10} \left(\frac{P}{P_0} \right)} \right]^{\frac{1}{2}}$$

ii) Magee carbon black t-plot equation:
$$t \text{ (nm)} = 0.1 \left(0.88 \left(\frac{P}{P_0} \right)^2 + 6.45 \left(\frac{P}{P_0} \right) + 2.98 \right)$$

The t-plot method correlates the quantity of nitrogen adsorbed to the statistical thickness (t) of the adsorbed layer. Internal SSA (or micropore SSA) were calculated as the difference between total (or BET) SSA and external SSA. Negative internal SSA were reported as zero.

2.2.2. Chemical characterisation

XPS - The surface chemistry of graphitic pellet samples was characterised by X-ray photoelectron spectroscopy (XPS), using a Kratos Axis Ultra DLD (Kratos Analytical, Manchester, UK) equipped with a monochromatic Al K α X-ray source (operated at 15 kV anode potential and 5 mA

emission current). During acquisition, the analyser was operated in ‘hybrid’ lens mode with the ‘slot’ entrance slit, which defines an analysis spot on the sample of $300\ \mu\text{m} \times 700\ \mu\text{m}$. Survey spectra between 1350 eV and -10 eV were collected with a pass energy of 160 eV, a step size of 1 eV, 200 ms dwell time, and 2 sweeps. Narrow scans were acquired for the C 1s, N 1s, and O 1s core levels with a pass energy of 20 eV, a step size of 100 meV, 500 ms dwell time, and 3 sweeps. A set of survey and narrow scans was acquired for 3 areas on each sample; no significant differences were observed between analysis areas. Charge neutralization with a low-energy electron source was not required as all the samples showed no evidence of charging. Transmission function corrected spectra were analysed using the CasaXPS software (Version 2.3.19) in conjunction with the average matrix relative sensitivity factors (AMRSF) published by the National Physical Laboratory (NPL) [54–56] in order to determine elemental composition. For all spectra, the Tougaard background type was employed, although a linear background was used when the decay of the inelastic background was dominant. As well as the powder samples, a highly ordered pyrolytic graphite crystal (HOPG, ZYA quality, Scanwel Ltd.) was prepared by cleaving with tape to reveal a fresh surface before immediately introducing it into vacuum. The HOPG was then sputtered with an Ar-cluster ion beam (Ar_{2000+} , 5 kV, $3 \times 3\ \text{mm}$, 90 s) which is anticipated to remove any adventitious and non-graphitic carbon, to achieve a graphitic sp^2 carbon surface.[57] Survey and high-resolution spectra were then acquired using the aforementioned parameters. The C 1s high resolution spectrum from HOPG was peak-fitted using the components detailed in **Table S1** in order to obtain an experimental lineshape for the asymmetric graphitic component. The C 1s high resolution spectra from the powder samples were also peak fitted using the components detailed in **Table S2**, which include graphitic C=C carbon, non-graphitic C-C carbon, carbon-oxygen species (C-O, C=O, O-C=O and a beta-shifted O-C=O), and loss features ($\pi - \pi^*$

transition and shake-up). The graphitic C=C carbon lineshape from the HOPG was used in fitting the powder samples C 1s spectra. Results from the fitting are shown in **Table S3**.

Raman spectroscopy – Confocal Raman spectroscopy was carried out using an inVia Qontor spectrometer (Renishaw, UK) on pelletised graphitic powders. A 532 nm laser was employed with a 100× objective lens (0.85 numerical aperture), with a power at the sample of 0.13 mW (1 % laser power) with a 2400 l/mm grating. Spectra were acquired with 2 s exposure for each measurement location. For each sample, spectra were recorded from 2 locations on the pellet, at each location a map with a 10 µm × 10 µm area (1 µm step size) was measured, for a total of 242 spectra per sample. Prior to peak fitting the spectra were processed in WiRE (Version 5.1) by removing the cosmic rays, subtracting the background and then normalizing the spectra to the peak with the highest intensity. Each spectrum was fitted individually to Lorentzian line shapes using WiRE and the relative intensities and FWHM were calculated for each spectrum. The standard deviation was also calculated to determine error bars.

3. Results and Discussion

3.1. Structural properties

The morphology and lateral flake size distribution of commercial graphitic materials, available in powder form, were evaluated using SEM. Sample preparation for SEM involved dispersing the powder in a solvent and drop-casting onto a pre-heated silicon substrate with a native oxide layer. The morphologies of the primary particles could be directly observed from the SEM images of the agglomerates/aggregates observed, as shown in **Figure 1**.

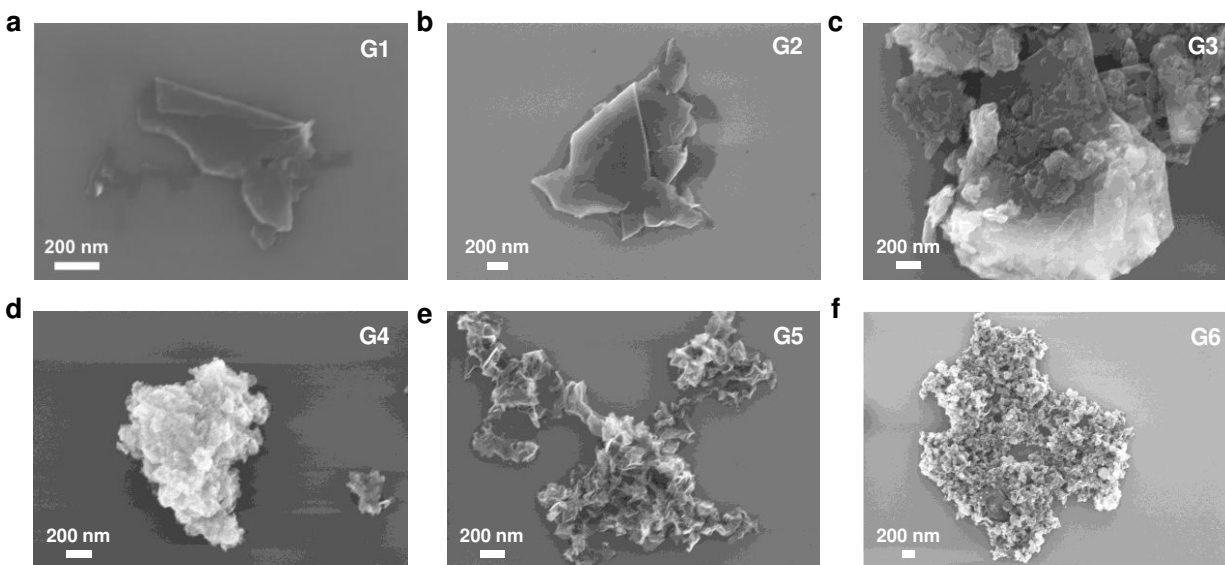


Figure 1. Morphology – (a-f) Scanning electron microscopy images of carbon materials deposited onto a silicon substrate with a native oxide layer, showing different morphologies (images were collected at different magnifications).

Materials produced *via* LPE methods (G1 and G2) exhibited typical flake-like morphologies commonly observed in layered materials. Materials produced *via* ball-milling exfoliation (G3 and G4) exhibited a more disordered structure with a high level of agglomeration/aggregation while graphitic carbons produced using bottom-up methods (G5 and G6) showed a non-planar morphology. Lateral sizes (defined as the average of the length and width) of numerous individual particles (> 200 for each type of material) were measured from SEM images to calculate their number distribution.[50] Flakes that were visibly agglomerated were excluded from the analysis as they were composed of multiple primary particles (definition in section 2.1 “materials”). However, for particles exhibiting possible aggregation/agglomeration (G5 and G6), the lateral sizes of the agglomerates/aggregates were measured rather than those of the individual isolated primary particles. Histograms representing the lateral size distributions for all six materials,

derived from SEM, are displayed in **Figure S1**, and lognormal-median lateral sizes for all samples are reported in **Table 2**, ranging from 90 nm to over 850 nm.

Although measurement of lateral flake size is extremely important for a variety of applications, [58,59] the thickness of the flakes is expected to impact the BET SSA and must therefore be carefully assessed. Thickness measurements were performed by AFM, with samples prepared by dispersing powders in a solvent and sonicating them in a ultrasonicator bath for 5 minutes, before drop-casting on pre-heated silicon substrates with a silica layer to minimize agglomeration. Typical images collected using AFM are reported in **Figure 2a** and **Figure S2** and displayed similar morphologies to those observed using SEM. Materials produced using bottom-up methods (G5 and G6) were particularly problematic to analyse with AFM because of their crumpled morphology, which does not result in flat 2D flakes. AFM height vs lateral size as measured using AFM for roughly 20 particles of each material are shown in **Figure 2b** and **Figure S3**, along with a linear fit of the data points. The lateral size-thickness correlation for materials produced *via* top-down exfoliation methods (G1 to G4) has previously been explained as a reduction in lateral flake size following a reduction in flake thickness due to fracturing of the basal plane.[19,60–62] Heights measured using AFM for these materials ranged from a few nanometers to over 100 nm, showing a large polydispersity and possible agglomeration in some cases where outliers were observed. Particles produced using bottom-up methods (G5 and G6) displayed a larger AFM height, with no flakes measured below 40 nm. This is due to the non-planar morphology of these particles, which means that the number of layers does not correlate directly to the height measured using AFM.

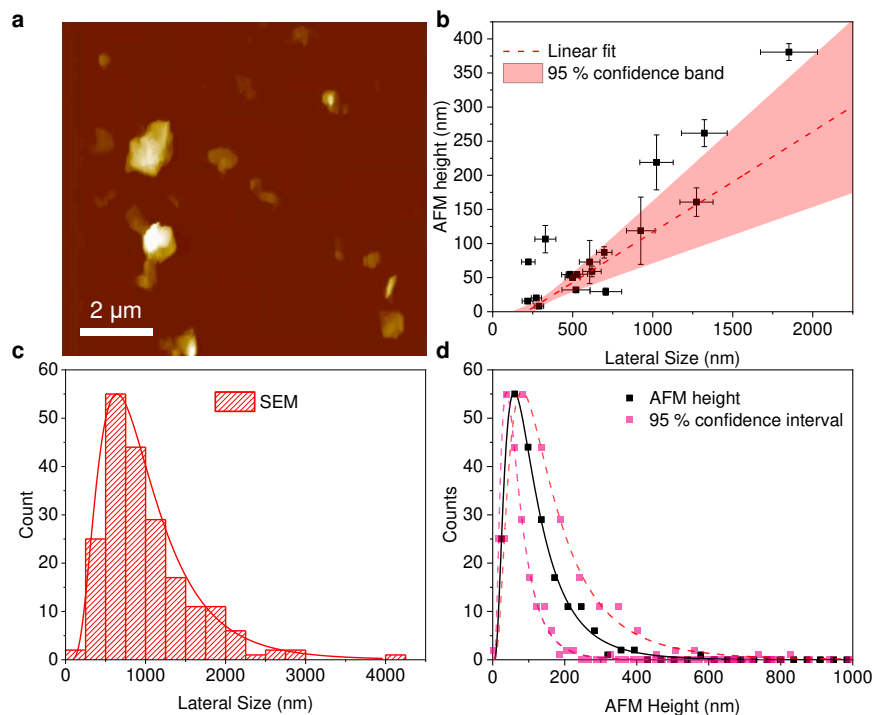


Figure 2. Thickness and Lateral size distribution of G1 – (a) Example of an AFM image (belonging to G1 graphitic powder) showing multiple graphitic flakes; (b) Recorded AFM height vs lateral size measured from AFM imaging, with associated error bars. The plot shows a linear fit of the lateral size versus thickness data points and the 95 % confidence interval of the fit; (c) Lateral size distribution derived from SEM images for the same sample fitted with a lognormal distribution; (d) AFM height distribution, as calculated from the lateral size distribution in (c), by applying the linear fit in (b).

Although AFM provides an accurate measurement of flake thickness for flat samples, it is typically a time-consuming technique, and so only a small number of flakes (~20) can be measured in a reasonable time-frame (~ 1 day). To provide a more robust measure of the distribution of flake thicknesses in the sample, the linear correlation between thickness and lateral size observed using AFM (**Figure 2c**) was employed to calculate height distributions from the larger particle

population measured with SEM (~200) as reported in **Figure 2d** and **Figure S4**. Clearly, because of the broad size distribution and confidence interval in the correlation, the results found for particle height exhibited a large polydispersity (lognormal median for AFM heights are reported in **Table 2**). In particular, the height measured for G5 and G6 produced using bottom-up methods is not truly representative of the real number of graphene layers in the particles. While some samples displayed obvious agglomeration (e.g. ball-milled or bottom-up graphitic materials), samples produced through LPE likely exhibited ordered re-aggregation in the z-plane during dispersion and deposition, resulting in larger height measurements from AFM.

Because of the intrinsic properties of carbon-based materials, Raman spectroscopy has been applied to gain information about chemistry, long range order, number of layers, and both the amount and type of defects.[19,63–65] For instance, the Raman D-peak vs G-peak intensity ratio (I_D/I_G) and the full width at half maximum of the G-peak (FWHM[G]) correlate to the number of defects present, which in turn can relate to the lateral flake size, due to the contribution of edge defects.[19] Likewise, the 2D-peak position ($\sim 2750\text{ cm}^{-1}$), intensity, and shape changes with the number of graphene layers and stacking configuration.[63] Hence, Raman spectra were measured for all samples to derive fundamental material properties which could then be compared with BET SSA values. Average Raman spectra for all samples, normalised to the intensity of the G-peak ($\sim 1580\text{ cm}^{-1}$), are reported in **Figure 3a** and in **Figure S5a**. All samples exhibited the typical vibrational modes for graphitic materials.[20,66–68] Intensity ratios for all samples derived from Raman spectroscopy are reported in **Table 2** and were derived from the analysis of over 200 spectra per sample.

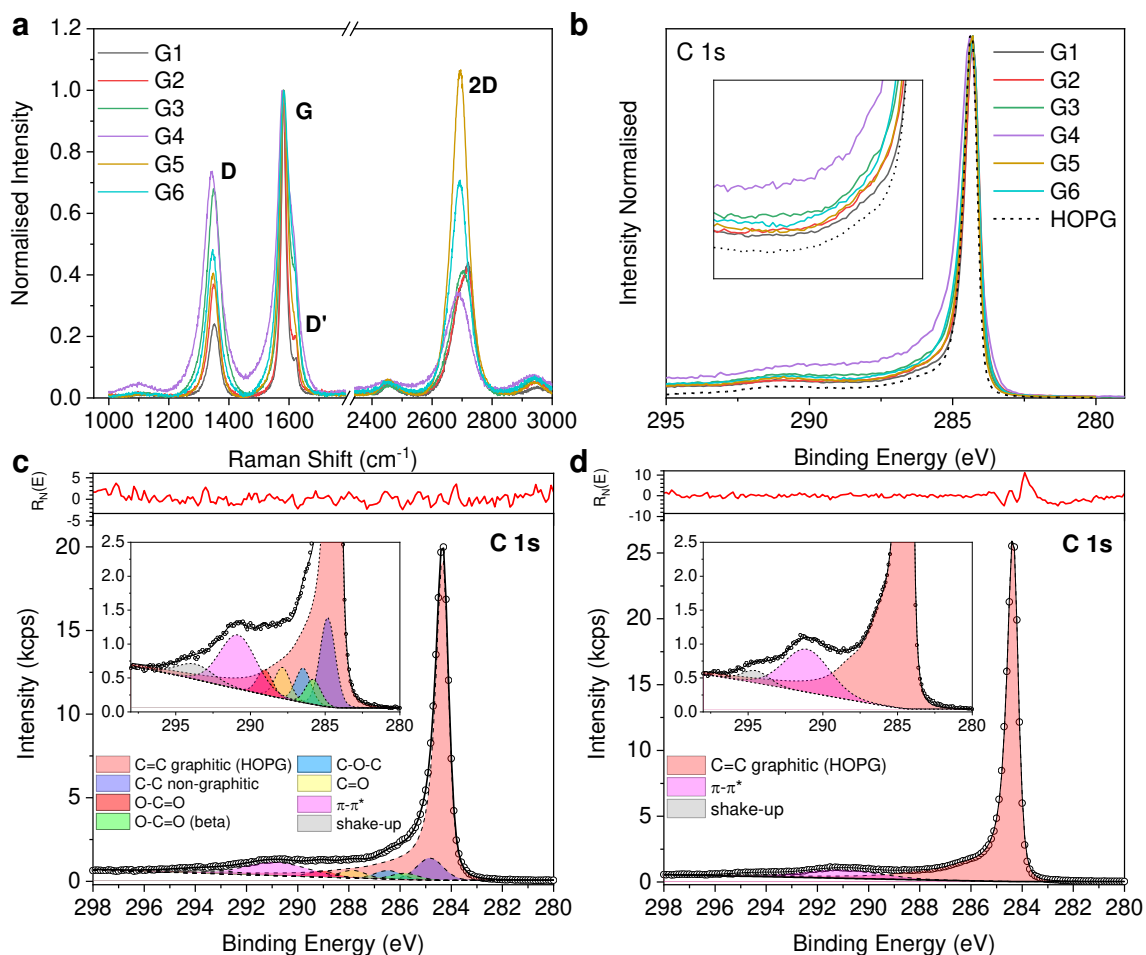


Figure 3. Disorder and Chemical Composition – (a) Raman spectra normalised to the G-peak intensity for all samples, (b) C 1s high resolution spectra with intensity normalised to the maximum intensity for all materials, the inset in the figure shows the broadening of the C 1s peak which can be correlated to an increased non-graphitic/graphitic carbon ratio, (c) C 1s high resolution spectrum for a functionalised graphitic material (sample G3) with peak fitted components (solid black line represents the fitted envelope and circles represent the raw data), (d) C 1s high resolution spectrum for pure HOPG, from which the C=C graphitic line shape has been used for the fitting of all other samples.

Table 2. Summary of structural and chemical properties *via* SEM, AFM, Raman spectroscopy and XPS analysis (uncertainties reported in **Table S4**).

Sample	SEM Lateral size (nm)	AFM height (nm)	I_D/I_G	I_{2D}/I_G	C (at%)	O (at%)	N (at%)	Fe (at%)	B (at%)	S (at%)
G1	877	98	0.25	0.44	97.4	2.4	0.1	--	--	0.1
G2	793	68	0.39	0.43	91.9	5.9	0.7	0.7	0.7	0.1
G3	438	57	0.73	0.44	94.6	4.7	0.7	--	--	--
G4	90	22	0.79	0.35	95.2	4.5	0.3	--	--	--
G5	215	85	0.42	1.12	98.1	1.9	--	--	--	0.1
G6	297	79	0.52	0.74	98.5	1.3	--	--	--	0.1

3.2. Chemical Characterisation

The chemical composition of the samples has been determined by XPS analysis. Typical XPS survey spectra are shown in **Figure S5b** from which relative elemental compositions were derived and reported in **Figure S5c**. All samples (analysed in pellet form) exhibited a large amount of carbon, with the presence of oxygen impurities determined to vary in content from roughly 6 at% to less than 2 at%. Some graphitic materials contained additional impurities, such as nitrogen (< 1 at%) and small amounts (< 1 at%) of iron, boron and sulfur (**Table 2** and **Figure S5c**). XPS was also used to analyse the chemical environment of the different atomic species present through analysis of the C 1s high resolution spectra (**Figure 3b**). **Figures 3c** and **3d** shows the C 1s peak fitting model used for the six powder samples and a highly oriented pyrolytic graphite (HOPG) reference sample respectively. The chemical components discussed here are fitted for every powder sample C 1s spectrum, using the constraints outlined in **Tables S1** and **S2**. For the powder samples, the main component observed at a binding energy of ~284.3 eV for all samples is

attributed to graphitic sp^2 carbon (aromatic rings) and exhibits an asymmetric peak characteristic of electrically conducting materials. A broad, low intensity π - π^* shake-up feature is also observed at a 5-6 eV higher binding energy than the graphitic peak, for all samples.[69] Between these graphitic carbon and π - π^* components, carbon-oxygen species are observed, such as ethers (C-O), ketones (C=O), and carboxyl (O-C=O and O-C=O (beta-shifted)) groups at ~286.5 eV, ~288.0 eV, ~289.9 eV and ~285.7 eV respectively.[70–73] In addition to the oxygen-containing moieties, a feature related to defects and other non-graphitic and non-oxidised carbon species at roughly 285 eV can be inferred from the shape of the C 1s spectra of the powder samples, in comparison to that of cleaned HOPG.[69,74] **Figure 3b** shows the normalised high-resolution C 1s spectra for the powder samples and the HOPG reference. There is a clear broadening observed in the spectra of the powder samples compared to the HOPG reference. The majority of the broadening manifests on the higher binding energy side where the defect and oxygen components are expected. The FWHM [C 1s] is generally observed to increase with increasing oxygen content (**Figure S5d**), except for G2 and G3 in which some of the oxygen may be associated to other impurities present (such as Fe and B, see **Table 2**). The different chemical components inferred from the peak-fitting of the C 1s spectra were also employed to calculate the ratio of non-graphitic/graphitic carbon, which is calculated as the ratio of the areas of the non-graphitic components (C-C non-graphitic, C-O-C, C=O, O-C=O) over the graphitic components (C=C graphitic).

3.3. Gas physisorption analysis and BET SSA

All the powder materials were obtained in dry form and degassed at two different temperatures of (i) 130 °C and (ii) 300 °C. This ensured the removal of all adsorbate species, while also investigating any major structural changes at higher degas temperatures. Nitrogen sorption isotherms at 77 K are reported in **Figure 4a**. Materials produced *via* LPE (G1 and G2) exhibited

typical isotherms for non-porous materials, while other materials generated isotherms with the presence of mesopores, micropores and/or relatively large external surface areas.[75] Nitrogen sorption isotherms were then employed to calculate BET SSA (**Figure 4b**). No major BET SSA differences were measured between the two degassing temperatures employed, suggesting no major structural changes at higher degas temperatures or removal of adsorbates. Samples produced through LPE (G1 and G2) exhibited relatively low BET SSA ($< 30 \text{ m}^2/\text{g}$), likely due to ordered re-aggregation of the flakes in dry form; other materials exhibited relatively high BET SSA ranging from roughly $100 \text{ m}^2/\text{g}$ to over $700 \text{ m}^2/\text{g}$.

Internal and external SSA were calculated for all materials using two different thickness-plot (t-plot) equations: i) Harkins and Jura and ii) Magee Carbon Black and are reported in **Figure S6**. The Carbon Black statistical thickness method (STSA) calculated the external SSA (STSA surface areas) higher than BET SSA for some of the samples. The Harkins and Jura equation produced better results for non-porous materials (G1 and G2 had near zero internal SSA) and is therefore more appropriate for these types of materials. Nevertheless, with both equations the BET SSA correlate linearly to external SSA and hence relationships elucidated in section 3.4 for BET SSA are valid for external SSA. Internal SSA could derive from: i) micropores present in amorphous regions of the samples (similarly to activated carbons), ii) the stacking arrangement of graphitic particles (platelets).

3.4. Correlation of physicochemical characterisation and BET SSA

To assess whether gas sorption measurements can provide useful information of the structural properties of commercially-available graphene/graphitic materials, the BET SSA for all six powders have been compared to structural and chemical parameters derived from previous

analyses. Firstly, BET SSAs were directly compared to the lateral size of graphitic flakes measured *via* SEM in **Figure 4c**.

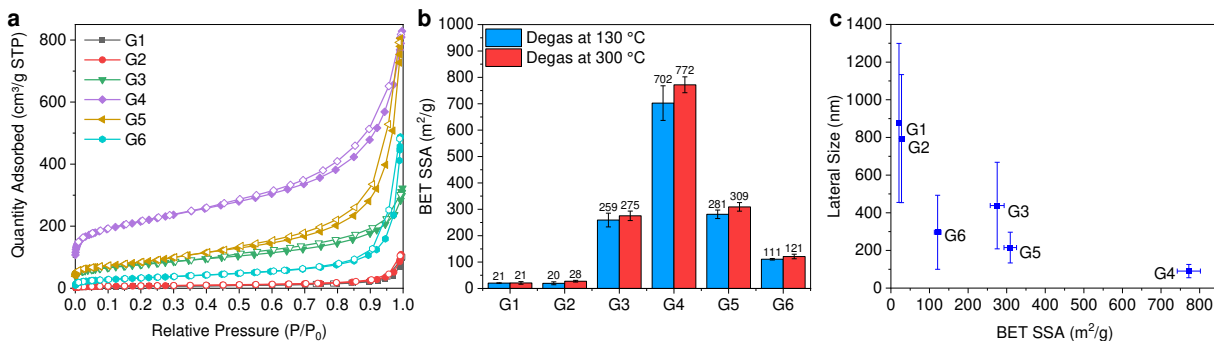


Figure 4. BET SSA vs lateral size – (a) Nitrogen sorption isotherms collected at 77 K for all graphitic materials degassed at 300 °C, open symbols represent desorption; (b) BET SSA derived from the nitrogen sorption isotherms for samples degassed at two different temperature (130 °C and 300 °C); (c) SEM lateral size (Lognormal median, with the mean standard deviation of the population distribution shown as error bars) vs BET SSA.

Generally, BET SSA increased with decreasing lateral size of graphitic flakes. However, lateral size is not expected to be the direct cause for a change in BET SSA in graphitic materials, due to negligible contributions of edge per unit mass. Instead, smaller lateral sizes are often associated with increasing non-graphitic/graphitic carbon ratio (because of larger amount of edge to bulk carbon) and/or thinner flakes, both of which are expected to directly affect BET SSA. The lateral size/ thickness correlation hypothesised above was investigated with AFM in **Figure 2**. Graphitic materials all showed similar thickness/lateral size correlations (similar aspect ratios). The same correlation observed for lateral size against BET SSA should therefore be observed when considering the thickness of the particles measured (shown here as AFM height) against BET SSA (**Figure S7a**). However, due to the large polydispersity in height measured using AFM analysis, and to the presence of aggregates and a crumpled morphology (in particular for materials produced

using bottom-up methods), the AFM height cannot be directly correlated to the number of graphitic layers of the primary particles (flakes). AFM height was also compared to other parameters in **Figure S7b** and **S7c**, decreasing with an increasing FWHM of the C 1s peak and increasing non-graphitic/graphitic carbon ratio, indicating either a potential correlation between thickness and the amount of non-graphitic carbon, i.e. thinner flakes may exhibit a higher number of defects, or potentially indicating that materials with higher non-graphitic carbon content do not aggregate/agglomerate to as great an extent.

Finally, the amount and type of disorder was analysed and their correlation with the BET SSA was evaluated. Firstly, disorder was assessed *via* Raman spectroscopy, where the FWHM of the Raman G-peak (FWHM[G]) is expected to scale with the lateral size of graphitic flakes.[19] A good correlation was observed between the FWHM[G] from Raman spectroscopy and the lateral size of the particles measured from SEM (**Figure 5a**), which points to the prevalence of edge-type defects over basal plane and vacancy defects. The ratio of intensities of the D- over G- peak (**Figure S8a**) showed a similar correlation, although this was not as expected for G5 and G6, produced using bottom-up methods. The disorder was then assessed by using i) I_D/I_G from Raman spectroscopy, ii) the FWHM of the C 1s peak from XPS and iii) the non-graphitic/graphitic carbon ratio derived from the peak fitting of the C 1s peaks from XPS (**Figure 5b** and **Figure S8c**). The different methods of quantification, for disorder and non-graphitic/graphitic carbon ratio showed a good correlation, giving us confidence in the analysis procedure employed. Both the amount of disorder and the non-graphitic/graphitic carbon ratio correlated to BET SSA in **Figures 5c**, **5d** and **Figure S8d**. Generally, samples with higher BET SSA exhibited a larger amount of disorder or non-graphitic carbon, which is in agreement with recently published work.[49]

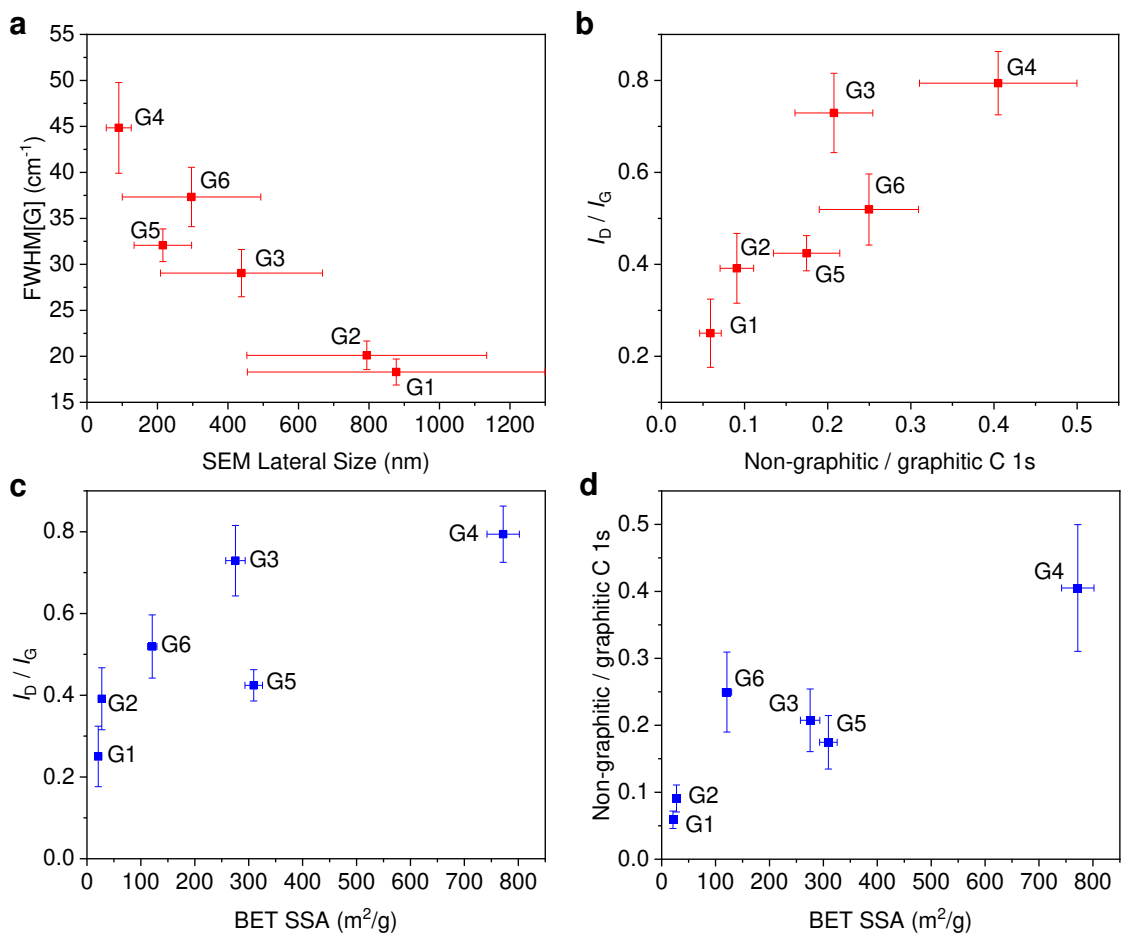


Figure 5. Correlation between disorder and BET SSA – (a) Full width at half maximum (FWHM) of the G-peak from Raman spectroscopy vs SEM lateral size; (b) Ratio of intensities of D- and G-peak from Raman spectroscopy vs non-graphitic/graphitic C 1s ratio derived from the peak fitting of C 1s spectra from XPS; (c) correlation between the level of disorder and the measured BET SSA; (d) correlation between the amount of non-graphitic carbon and the BET SSA.

4. Conclusions Nitrogen sorption analysis has been shown to hold promise as a relatively high-throughput method to determine the properties of graphitic powder samples. However, an understanding of the accuracy of this method is extremely important, as SSA determined by BET will be employed in REACH regulation of chemicals in the European Union, specifically for the classification of nanoforms of substances. With powders containing few-layer graphene and

graphitic particles now being produced on the large scale of tonnes per year, the knowledge of the strengths and limitations of measuring the SSA of these commercially-available materials with BET will be paramount.

From the materials studied here, powders of graphitic materials with higher BET SSA values tended to contain particles with smaller lateral size (as measured using SEM), a higher non-graphitic/graphitic carbon ratio (derived from XPS) and higher disorder (revealed using Raman spectroscopy).

Heights of the particles were measured from AFM images for all samples but were not always truly representative of the primary particle thickness due to the presence of aggregates/agglomerates or a crumpled morphology, the latter particularly for particles produced through bottom-up production processes. Similarly, BET SSA values are likely to overestimate the number of layers of the primary particles due to the presence of aggregates, thus this method could not be employed to directly derive the average number of layers of graphitic flakes.

The extent of aggregation depends upon the production method and nature of the material analysed, which must be taken into careful consideration when employing nitrogen physisorption for the analysis of graphitic materials. From our study it could be hypothesised that materials with a higher non-graphitic/graphitic carbon ratio or a greater level of disorder, exhibited a lower degree of aggregation and for these materials the BET SSA is likely to be more representative of the true thickness of the graphitic primary particles.

Supplementary data

Supplementary data to this article can be found online at XXX.

Supplementary information includes: Histograms showing SEM lateral size distributions for all samples, AFM images for all materials, AFM lateral size/ height correlations for all samples, AFM height distributions derived from SEM lateral size distributions for all samples, Raman and XPS spectra for all materials, correlations between structural and chemical properties and BET SSA, internal and external specific surface areas, table summarising structural and chemical properties with associated uncertainties, fitting model employed for C 1s for XPS analysis, which was used to derive the non-graphitic/graphitic carbon ratios.

Author Contributions

The manuscript was written through contributions of all authors. Experiments were designed and conceived by SM, KP, BB and AJP. Some materials were supplied by KK. Measurements performed by SM (BET SSA, Raman spectroscopy, SEM, XPS), PT (AFM) and BR (XPS experiments and data analysis). All authors have given approval to the final version of the manuscript.

Funding Sources

The National Measurement System (NMS) of the Department for Business, Energy and Industrial Strategy (BEIS), UK, (project #122464, Metrology for High Energy Density Batteries)

Acknowledgments

The authors would like to thank Haydale Ltd, Thomas Swan & Co. Ltd and Cambridge Nanosystems Ltd for supplying some of the graphitic materials employed in this study. The authors

would also like to thank Dr Rinaldo Raccichini and Dr Alexander Shard for discussions concerning the manuscript.

References

- [1] A.J. Pollard, C.A. Clifford, Terminology: the first step towards international standardisation of graphene and related 2D materials, *J. Mater. Sci.* 52 (2017) 13685–13688. <https://doi.org/10.1007/s10853-017-1567-7>.
- [2] D. Long, W. Li, W. Qiao, J. Miyawaki, S.-H. Yoon, I. Mochida, et al., Graphitization behaviour of chemically derived graphene sheets, *Nanoscale*. 3 (2011) 3652–3656. <https://doi.org/10.1039/c1nr10409h>.
- [3] J.C. Meyer, A.K. Geim, M.I. Katsnelson, K.S. Novoselov, T.J. Booth, S. Roth, The structure of suspended graphene sheets, *Nature*. 446 (2007) 60–63. <https://doi.org/10.1038/nature05545>.
- [4] A.K. Geim, K.S. Novoselov, The rise of graphene, in: *Nanosci. Technol.*, Nature Publishing Group, Manchester, 2009: pp. 11–19. https://doi.org/10.1142/9789814287005_0002.
- [5] K.S. Novoselov, V.I. Fal’ko, L. Colombo, P.R. Gellert, M.G. Schwab, & K. Kim, A roadmap for graphene, *Nature*. 490 (2012) 192–200. <https://doi.org/10.1038/nature11458>.
- [6] A.C. Ferrari, F. Bonaccorso, V. Fal’ko, K.S. Novoselov, S. Roche, P. Bøggild, et al., Science and technology roadmap for graphene, related two-dimensional crystals, and hybrid systems, *Nanoscale*. 7 (2015) 4598–4810. <https://doi.org/10.1039/C4NR01600A>.
- [7] R. Raccichini, A. Varzi, S. Passerini, B. Scrosati, The role of graphene for electrochemical energy storage, *Nat. Mater.* 14 (2015) 271–279. <https://doi.org/10.1038/nmat4170>.
- [8] J.N. Coleman, M. Lotya, A. O’Neill, S.D. Bergin, P.J. King, U. Khan, et al., Two-dimensional nanosheets produced by liquid exfoliation of layered materials, *Science* (80-.). 331 (2011) 568–571. <https://doi.org/10.1126/science.1194975>.
- [9] A.K. Geim, M. Lotya, A. O’Neill, S.D. Bergin, P.J. King, U. Khan, et al., Graphene: Status

- and Prospects, *Science* (80-.). 324 (2011) 1530–1534.
<https://doi.org/10.1126/science.1158877>.
- [10] W. Ren, H.-M. Cheng, The global growth of graphene, *Nat. Nanotechnol.* 9 (2014) 726–730. <https://doi.org/10.1038/nnano.2014.229>.
- [11] I.-Y. Jeon, H.-J. Choi, S.-M. Jung, J.-M. Seo, M.-J. Kim, L. Dai, et al., Large-Scale Production of Edge-Selectively Functionalized Graphene Nanoplatelets via Ball Milling and Their Use as Metal-Free Electrocatalysts for Oxygen Reduction Reaction, *J. Am. Chem. Soc.* 135 (2013) 1386–1393. <https://doi.org/10.1021/ja3091643>.
- [12] C.R. Herron, K.S. Coleman, R.S. Edwards, B.G. Mendis, Simple and scalable route for the ‘bottom-up’ synthesis of few-layer graphene platelets and thin films, *J. Mater. Chem.* 21 (2011) 3378. <https://doi.org/10.1039/c0jm03437a>.
- [13] Graphene companies: the comprehensive list | Graphene-Info, (n.d.). <https://www.graphene-info.com/companies> (accessed September 13, 2019).
- [14] C. Mattevi, H. Kim, M. Chhowalla, A review of chemical vapour deposition of graphene on copper, *J. Mater. Chem.* 21 (2011) 3324–3334. <https://doi.org/10.1039/C0JM02126A>.
- [15] R. Raccichini, A. Varzi, D. Wei, S. Passerini, Critical Insight into the Relentless Progression Toward Graphene and Graphene-Containing Materials for Lithium-Ion Battery Anodes, *Adv. Mater.* 29 (2017) 1603421. <https://doi.org/10.1002/adma.201603421>.
- [16] A.P. Kauling, A.T. Seefeldt, D.P. Pisoni, R.C. Pradeep, R. Bentini, R.V.B. Oliveira, et al., The Worldwide Graphene Flake Production, *Adv. Mater.* 30 (2018) 1803784. <https://doi.org/10.1002/adma.201803784>.
- [17] P. Bøggild, The war on fake graphene, *Nature.* 562 (2018) 502–503. <https://doi.org/10.1038/d41586-018-06939-4>.

- [18] A. Bianco, H.M. Cheng, T. Enoki, Y. Gogotsi, R.H. Hurt, N. Koratkar, et al., All in the graphene family - A recommended nomenclature for two-dimensional carbon materials, *Carbon N. Y.* 65 (2013) 1–6. <https://doi.org/10.1016/j.carbon.2013.08.038>.
- [19] C. Backes, K. Paton, D. Hanlon, S. Yuan, M.K.- Nanoscale, U. 2016, Spectroscopic metrics allow in situ measurement of mean size and thickness of liquid-exfoliated few-layer graphene nanosheets, *Nanoscale.* 8 (2016) 4311–4323. <https://doi.org/10.1039/c5nr08047a>.
- [20] A.J. Pollard, B. Brennan, H. Stec, B.J. Tyler, M.P. Seah, I.S. Gilmore, et al., Quantitative characterization of defect size in graphene using Raman spectroscopy, *Appl. Phys. Lett.* 105 (2014) 253107. <https://doi.org/10.1063/1.4905128>.
- [21] F. Tuinstra, J.L. Koenig, Raman Spectrum of Graphite, *J. Chem. Phys.* 53 (1970) 1126–1130. <https://doi.org/10.1063/1.1674108>.
- [22] T. Ohba, A. Takase, Y. Ohyama, H. Kanoh, Grand canonical Monte Carlo simulations of nitrogen adsorption on graphene materials with varying layer number, *Carbon N. Y.* 61 (2013) 40–46. <https://doi.org/10.1016/J.CARBON.2013.04.061>.
- [23] S. Brunauer, P.H. Emmett, E. Teller, Adsorption of Gases in Multimolecular Layers, *J. Am. Chem. Soc.* 60 (1938) 309–319. <https://doi.org/10.1021/ja01269a023>.
- [24] ECHA, Appendix for nanoforms applicable to the Guidance on Registration and substance identification, 2019, (2019).
- [25] F. Guo, M. Creighton, Y. Chen, R. Hurt, I. Külaots, Porous structures in stacked, crumpled and pillared graphene-based 3D materials, *Carbon N. Y.* 66 (2014) 476–484. <https://doi.org/10.1016/J.CARBON.2013.09.024>.
- [26] Y. Li, P. Zhang, Q. Du, X. Peng, T. Liu, Z. Wang, et al., Adsorption of fluoride from aqueous solution by graphene, *J. Colloid Interface Sci.* 363 (2011) 348–354.

- <https://doi.org/10.1016/J.JCIS.2011.07.032>.
- [27] H. Gao, K. Zhu, G. Hu, C. Xue, Large-scale graphene production by ultrasound-assisted exfoliation of natural graphite in supercritical CO₂/H₂O medium, *Chem. Eng. J.* 308 (2017) 872–879. <https://doi.org/10.1016/J.CEJ.2016.09.132>.
- [28] X. Liu, M. Zheng, K. Xiao, Y. Xiao, C. He, H. Dong, et al., Simple, green and high-yield production of single- or few-layer graphene by hydrothermal exfoliation of graphite, *Nanoscale*. 6 (2014) 4598–4603. <https://doi.org/10.1039/C3NR06219H>.
- [29] Y. Si, E.T. Samulski, Exfoliated Graphene Separated by Platinum Nanoparticles, *Chem. Mater.* 20 (2008) 6792–6797. <https://doi.org/10.1021/cm801356a>.
- [30] Y. Zhu, T. Cao, C. Cao, X. Ma, X. Xu, Y. Li, A general synthetic strategy to monolayer graphene, *Nano Res.* 11 (2018) 3088–3095. <https://doi.org/10.1007/s12274-017-1703-3>.
- [31] Hannes C. Schniepp, J.-L. Li, M.J. McAllister, H. Sai, Margarita Herrera-Alonso, § Douglas H. Adamson, et al., Functionalized Single Graphene Sheets Derived from Splitting Graphite Oxide, *Phys. Chem. B.* 110 (2006) 8535–8539. <https://doi.org/10.1021/JP060936F>.
- [32] L. Chen, C. Batchelor-McAuley, B. Rasche, C. Johnston, N. Hindle, R.G. Compton, Surface area measurements of graphene and graphene oxide samples: Dopamine adsorption as a complement or alternative to methylene blue?, *Appl. Mater. Today*. 18 (2020) 100506. <https://doi.org/10.1016/J.APMT.2019.100506>.
- [33] S. Wang, Z.H. Zhu, A. Coomes, F. Haghseresht, G.Q. Lu, The physical and surface chemical characteristics of activated carbons and the adsorption of methylene blue from wastewater, *J. Colloid Interface Sci.* 284 (2005) 440–446. <https://doi.org/10.1016/J.JCIS.2004.10.050>.
- [34] Y. Li, Q. Du, T. Liu, X. Peng, J. Wang, J. Sun, et al., Comparative study of methylene blue

- dye adsorption onto activated carbon, graphene oxide, and carbon nanotubes, *Chem. Eng. Res. Des.* 91 (2013) 361–368. <https://doi.org/10.1016/j.cherd.2012.07.007>.
- [35] K. Kaneko, C. Ishii, M. Ruike, H. kuwabara, Origin of superhigh surface area and microcrystalline graphitic structures of activated carbons, *Carbon N. Y.* 30 (1992) 1075–1088. [https://doi.org/10.1016/0008-6223\(92\)90139-N](https://doi.org/10.1016/0008-6223(92)90139-N).
- [36] E. Raymundo-Piñero, K. Kierzek, J. Machnikowski, F. Béguin, Relationship between the nanoporous texture of activated carbons and their capacitance properties in different electrolytes, *Carbon N. Y.* 44 (2006) 2498–2507. <https://doi.org/10.1016/j.carbon.2006.05.022>.
- [37] Z. Zhang, H.C. Schniepp, D.H. Adamson, Characterization of graphene oxide: Variations in reported approaches, *Carbon N. Y.* 154 (2019) 510–521. <https://doi.org/10.1016/j.carbon.2019.07.103>.
- [38] S. Park, J. An, J.R. Potts, A. Velamakanni, S. Murali, R.S. Ruoff, Hydrazine-reduction of graphite- and graphene oxide, *Carbon N. Y.* 49 (2011) 3019–3023. <https://doi.org/10.1016/J.CARBON.2011.02.071>.
- [39] B. Xu, S. Yue, Z. Sui, X. Zhang, S. Hou, G. Cao, et al., What is the choice for supercapacitors: graphene or graphene oxide?, *Energy Environ. Sci.* 4 (2011) 2826. <https://doi.org/10.1039/c1ee01198g>.
- [40] S. Stankovich, D.A. Dikin, R.D. Piner, K.A. Kohlhaas, A. Kleinhammes, Y. Jia, et al., Synthesis of graphene-based nanosheets via chemical reduction of exfoliated graphite oxide, *Carbon N. Y.* 45 (2007) 1558–1565. <https://doi.org/10.1016/J.CARBON.2007.02.034>.
- [41] B. Zhao, P. Liu, Y. Jiang, D. Pan, H. Tao, J. Song, et al., Supercapacitor performances of

- thermally reduced graphene oxide, *J. Power Sources*. 198 (2012) 423–427.
<https://doi.org/10.1016/J.JPOWSOUR.2011.09.074>.
- [42] Y. Zhang, S. Wang, L. Li, K. Zhang, J. Qiu, M. Davis, et al., Tuning electrical conductivity and surface area of chemically-exfoliated graphene through nanocrystal functionalization, *Mater. Chem. Phys.* 135 (2012) 1057–1063.
<https://doi.org/10.1016/J.MATCHEMPHYS.2012.06.014>.
- [43] S.-H. Park, H.-K. Kim, S.-B. Yoon, C.-W. Lee, D. Ahn, S.-I. Lee, et al., Spray-Assisted Deep-Frying Process for the In Situ Spherical Assembly of Graphene for Energy-Storage Devices, *Chem. Mater.* 27 (2015) 457–465. <https://doi.org/10.1021/cm5034244>.
- [44] L.-Z. Fan, J.-L. Liu, R. Ud-Din, X. Yan, X. Qu, The effect of reduction time on the surface functional groups and supercapacitive performance of graphene nanosheets, *Carbon N. Y.* 50 (2012) 3724–3730. <https://doi.org/10.1016/J.CARBON.2012.03.046>.
- [45] S.J. Yang, T. Kim, H. Jung, C.R. Park, The effect of heating rate on porosity production during the low temperature reduction of graphite oxide, *Carbon N. Y.* 53 (2013) 73–80.
<https://doi.org/10.1016/J.CARBON.2012.10.032>.
- [46] J. Park, Y.S. Cho, S.J. Sung, M. Byeon, S.J. Yang, C.R. Park, Characteristics tuning of graphene-oxide-based-graphene to various end-uses, *Energy Storage Mater.* 14 (2018) 8–21. <https://doi.org/10.1016/j.ensm.2018.02.013>.
- [47] I.-Y. Jeon, Y.-R. Shin, G.-J. Sohn, H.-J. Choi, S.-Y. Bae, J. Mahmood, et al., Edge-carboxylated graphene nanosheets via ball milling., *Proc. Natl. Acad. Sci. U. S. A.* 109 (2012) 5588–93. <https://doi.org/10.1073/pnas.1116897109>.
- [48] Y. Chen, J. Fitz Gerald, L.T. Chadderton, L. Chaffron, Nanoporous carbon produced by ball milling, *Appl. Phys. Lett.* 74 (1999) 2782–2784. <https://doi.org/10.1063/1.124012>.

- [49] A. Kovtun, E. Treossi, N. Mirotta, A. Scidà, A. Liscio, M. Christian, et al., Benchmarking of graphene-based materials: Real commercial products versus ideal graphene, *2D Mater.* 6 (2019). <https://doi.org/10.1088/2053-1583/aafc6e>.
- [50] A.J. Pollard, K.R. Paton, C.A. Clifford, E.J. Legge, A. Oikonomou, S. Haigh, et al., NPL Good Practice Guide No. 145: Characterisation of the Structure of Graphene, 2017.
- [51] J. Rouquerol, P. Llewellyn, F. Rouquerol, Is the bet equation applicable to microporous adsorbents?, *Stud. Surf. Sci. Catal.* 160 (2007) 49–56. [https://doi.org/10.1016/S0167-2991\(07\)80008-5](https://doi.org/10.1016/S0167-2991(07)80008-5).
- [52] W.D. Harkins, G. Jura, Surfaces of Solids. XII. An Absolute Method for the Determination of the Area of a Finely Divided Crystalline Solid, *J. Am. Chem. Soc.* 66 (1944) 1362–1366. <https://doi.org/10.1021/ja01236a047>.
- [53] R.W. Magee, Evaluation of the External Surface Area of Carbon Black by Nitrogen Adsorption, *Rubber Chem. Technol.* 68 (1995) 590–600. <https://doi.org/10.5254/1.3538760>.
- [54] NPL, Average Matrix Relative Sensitivity Factors (AMRSFs) for X-ray Photoelectron Spectroscopy (XPS), 1 (2006) 1–10.
- [55] M.. Seah, I. Gilmore, S.. Spencer, Quantitative XPS: I. Analysis of X-ray photoelectron intensities from elemental data in a digital photoelectron database, *J. Electron Spectros. Relat. Phenomena.* 120 (2001) 93–111. [https://doi.org/10.1016/S0368-2048\(01\)00311-5](https://doi.org/10.1016/S0368-2048(01)00311-5).
- [56] S. Tanuma, Summary of ISO/TC 201 Standard: XX ISO 18118: 2004 – Surface chemical analysis – Auger electron spectroscopy and X-ray photoelectron spectroscopy – Guide to the use of experimentally determined relative sensitivity factors for the quantitative analysis of homogeneous materials, *Surf. Interface Anal.* 38 (2006) 178–180.

<https://doi.org/10.1002/sia.2177>.

- [57] B.J. Tyler, B. Brennan, H. Stec, T. Patel, L. Hao, I.S. Gilmore, et al., Removal of Organic Contamination from Graphene with a Controllable Mass-Selected Argon Gas Cluster Ion Beam, *J. Phys. Chem. C.* 119 (2015) 17836–17841. <https://doi.org/10.1021/acs.jpcc.5b03144>.
- [58] M. Zhao, D.-B. Xiong, Z. Tan, G. Fan, Q. Guo, C. Guo, et al., Lateral size effect of graphene on mechanical properties of aluminum matrix nanolaminated composites, *Scr. Mater.* 139 (2017) 44–48. <https://doi.org/10.1016/J.SCRIPTAMAT.2017.06.018>.
- [59] S.G. Prolongo, A. Jiménez-Suárez, R. Moriche, A. Ureña, Graphene nanoplatelets thickness and lateral size influence on the morphology and behavior of epoxy composites, *Eur. Polym. J.* 53 (2014) 292–301. <https://doi.org/10.1016/J.EURPOLYMJ.2014.01.019>.
- [60] C. Backes, D. Campi, B.M. Szydłowska, K. Synnatschke, E. Ojala, F. Rashvand, et al., Equipartition of Energy Defines the Size–Thickness Relationship in Liquid-Exfoliated Nanosheets, *ACS Nano.* 13 (2019) 7050–7061. <https://doi.org/10.1021/acsnano.9b02234>.
- [61] A. Liscio, K. Kouroupis-Agalou, X.D. Betriu, A. Kovtun, E. Treossi, N.M. Pugno, et al., Evolution of the size and shape of 2D nanosheets during ultrasonic fragmentation, *2D Mater.* 4 (2017) 025017. <https://doi.org/10.1088/2053-1583/aa57ff>.
- [62] K. Kouroupis-Agalou, A. Liscio, E. Treossi, L. Ortolani, V. Morandi, N.M. Pugno, et al., Fragmentation and exfoliation of 2-dimensional materials: a statistical approach, *Nanoscale.* 6 (2014) 5926–5933. <https://doi.org/10.1039/C3NR06919B>.
- [63] A.C. Ferrari, D.M. Basko, Raman spectroscopy as a versatile tool for studying the properties of graphene, *Nat. Nanotechnol.* 8 (2013) 235–246. <https://doi.org/10.1038/nnano.2013.46>.
- [64] L.M. Malard, M.A. Pimenta, G. Dresselhaus, M.S. Dresselhaus, Raman spectroscopy in

- graphene, *Phys. Rep.* 473 (2009) 51–87. <https://doi.org/10.1016/J.PHYSREP.2009.02.003>.
- [65] A.C. Ferrari, Raman spectroscopy of graphene and graphite: Disorder, electron–phonon coupling, doping and nonadiabatic effects, *Solid State Commun.* 143 (2007) 47–57. <https://doi.org/10.1016/J.SSC.2007.03.052>.
- [66] A.C. Ferrari, J. Robertson, Interpretation of Raman spectra of disordered and amorphous carbon, *Phys. Rev. B.* 61 (2000) 14095–14107. <https://doi.org/10.1103/PhysRevB.61.14095>.
- [67] L.G. Cançado, A. Jorio, E.H.M. Ferreira, F. Stavale, C.A. Achete, R.B. Capaz, et al., Quantifying defects in graphene via Raman spectroscopy at different excitation energies, *Nano Lett.* 11 (2011) 3190–3196. <https://doi.org/10.1021/nl201432g>.
- [68] E.J. Legge, M. Ahmad, C.T.G. Smith, B. Brennan, C.A. Mills, V. Stolojan, et al., Physicochemical characterisation of reduced graphene oxide for conductive thin films, *RSC Adv.* 8 (2018) 37540–37549. <https://doi.org/10.1039/C8RA08849G>.
- [69] H. Estrade-Szwarckopf, XPS photoemission in carbonaceous materials: A “defect” peak beside the graphitic asymmetric peak, *Carbon N. Y.* 42 (2004) 1713–1721. <https://doi.org/10.1016/J.CARBON.2004.03.005>.
- [70] D. Briggs, M.P. Seah, *Practical surface analysis: by auger and x-ray photoelectron spectroscopy*, Wiley-Blackwell, Chicester, 1983. <https://doi.org/10.1002/sia.740060611>.
- [71] C.D. Wanger, W.M. Riggs, L.E. Davis, J.F. Moulder, G.E. Muilenberg, *Handbook of X-ray photoelectron spectroscopy*, Eden Prairie, Minnesota, 1979. <https://doi.org/10.1002/sia.740030412>.
- [72] G. Beamson, High Resolution XPS of Organic Polymers, *Sci. ESCA 300 Database.* (1992). <https://ci.nii.ac.jp/naid/10003489274/> (accessed October 2, 2019).

- [73] A.P. Pijpers, R.J. Meier, Oxygen-induced secondary substituent effects in polymer XPS spectra, *J. Electron Spectros. Relat. Phenomena.* 43 (1987) 131–137.
[https://doi.org/10.1016/0368-2048\(87\)80025-7](https://doi.org/10.1016/0368-2048(87)80025-7).
- [74] J.C. Lascovich, R. Giorgi, S. Scaglione, Evaluation of the sp^2/sp^3 ratio in amorphous carbon structure by XPS and XAES, *Appl. Surf. Sci.* 47 (1991) 17–21.
[https://doi.org/10.1016/0169-4332\(91\)90098-5](https://doi.org/10.1016/0169-4332(91)90098-5).
- [75] K.S.W. Sing, D.H. Everett, R.A.W. Haul, L. Moscou, R.S. Pierotti, J. Rouquerol, et al., Reporting physisorption data for gas/solid systems with special reference to the determination of surface area and porosity, *Pure Appl. Chem.* 57 (1985) 603–619.
<https://doi.org/10.1351/pac198557040603>.